Robotics and Autonomous Systems 197 (2026) 105283

Contents lists available at ScienceDirect

Robotics and Autonomous Systems

journal homepage: www.elsevier.com/locate/robot

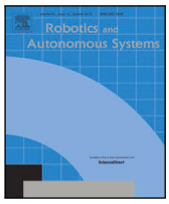

The FriûlBot dataset: Experimental validation of an autonomous ground robot for vineyard 3D mapping

Diego Tiozzo Fasiolo, Lorenzo Scalera *, Eleonora Maset, Alessandro Gasparetto

Polytechnic Department of Engineering and Architecture, University of Udine, via delle Scienze, 206, 33100, Udine, Italy

ARTICLE INFO

Keywords:
Robotics
3D mapping
SLAM
Precision agriculture
Autonomous navigation

ABSTRACT

In this paper, we present the FriûlBot open-source dataset, collected by an autonomous mobile robot for vineyard 3D mapping and monitoring. The dataset is designed to provide a reference testbed for the development and benchmarking of localization, mapping, and multi-sensor data fusion algorithms. It includes detailed information on the robot status, point clouds of the vineyard, and multispectral images, offering valuable resources for future research on autonomous robotic systems in agriculture. The mobile robot employed for the dataset acquisition is capable of autonomously navigating, reaching GNSS way points, and building a map of the canopy integrating geometric and multispectral data. The navigation and mapping approach proposed in this work is based on a SLAM algorithm that integrates multiple odometry sources, and is designed for agricultural environments with plants arranged in rows, e.g., vineyards and orchards. The performance of the proposed mobile robot and navigation approach are tested during an extensive experimental campaign in a vineyard of University of Udine (Italy). During the tests, the robot successfully navigates along several vineyard rows, building point clouds of the environment that are merged with data regarding multiple vegetation indexes. The experimental results confirm the reliability of the autonomous mobile robot and the potential of the proposed dataset to foster further advances in robotics for vineyard 3D mapping.

1. Introduction

Nowadays, the demand for automation in agriculture is increasing, and innovative technologies are required for analyzing and monitoring plants and crops, thus optimizing farming productivity [1,2]. In this context, ground robots can be used to map and monitor the spatial variability of the fields, by collecting data from different perspectives [3,4]. Among the types of maps that can be generated using a mobile robot, 3D point clouds enable the extraction of parameters such as height and volume of plants. Furthermore, mobile robots offer a distinct point of view for integrating data that can also be acquired by unmanned aerial vehicles [5,6].

The development of a robotic platform suited for agricultural environments (e.g., vineyards) involves the integration of specific hardware and software [7]. To ensure a consistent monitoring of the plants, mobile robots should be provided with cutting-edge navigation and mapping techniques [8,9]. Planning a path free from collisions with obstacles in the vineyard, e.g., leaves, branches, trunks, and human workers, is one of the main problems that an autonomous mobile robot has to solve [10]. For instance, the approach in [11] uses a volumetric representation of the environment as an input to generate a feasible path that ensures the mobile robot to cover the entire field without gaps or overlaps. A topological path-planning approach is adopted in [12] to make the Thorvald robotic platform follow similar paths in repeated surveys, whereas the skid-steered robot in [13] exploits a path-planning technique specifically designed for steep slope vineyards. Furthermore, a robotic platform capable of generating paths with a data-driven approach given the occupancy grid of a vineyard is proposed in [14], whereas the collision-avoidance strategy presented in [15] aims at avoiding damages of the grapevines while smoothing the trajectories of the robot in a vineyard.

To correctly follow the planned path, a proper localization of the robot, i.e., the estimate of its 6-degree-of-freedom (DOF) pose, is needed [3]. Numerous examples in the literature present robots utilizing Global Navigation Satellite System (GNSS) improved with Real-Time Kinematic (RTK) solutions in conjunction with Inertial Measurement Units (IMUs) [21,22]. However, the GNSS reliability in vineyards can be compromised by signal obstruction and multi-path reflection. Furthermore, IMUs could lead to noisy path estimations as a consequence of the vehicle vibrations in rough agricultural terrains. The additional integration of LiDAR- (Light Detection and Ranging) or visual-SLAM (Simultaneous Localization and Mapping) techniques can

* Corresponding author.
E-mail address: lorenzo.scalera@uniud.it (L. Scalera).

https://doi.org/10.1016/j.robot.2025.105283
Received 24 October 2024; Received in revised form 7 November 2025; Accepted 5 December 2025
Available online 5 December 2025

Table 1
Overview on cutting-edge mobile robots for vineyard mapping and monitoring.

Author	Year	Ref.	Path planning approach	Localization strategy	Mapping application
Aguiar et al.	2022	[16]	✗	3D LiDAR SLAM	3D reconstruction as a voxel grid map (based on LiDAR data)
Clamens et al.	2021	[17]	✗	✗	3D scans and multispectral images registration
Crocetti et al.	2023	[18]	✗	Visual-Inertial SLAM, 3D LiDAR-Inertial SLAM	2D georeferenced NDVI maps obtained using images and GNSS positions
Fernández-Novales	2021	[19]	Row following only (based on ultrasound data)	GNSS-based	2D georeferenced maps of leaf water potential
Marzoa Tanco et al.	2023	[20]	Row following only (based on LiDAR data)	Visual SLAM	3D reconstruction as a point cloud (based on stereo camera)
Polvara et al.	2023	[12]	Topological path planning	3D LiDAR-Inertial SLAM	3D reconstruction as a point cloud (based on LiDAR data)
Proposed approach			Global path planning and collision avoidance	LiDAR SLAM (based on LiDAR, IMU, wheels odometry, and GNSS)	3D reconstruction as a point cloud (based on LiDAR data) with vegetation indexes associated with the points

Fig. 1. The mobile robot in vineyard used to collect the FriûlBot dataset.

provide a more robust solution for the localization of the robot [18,23]. A classical LiDAR SLAM approach originally designed for indoor environments and adapted for vineyard navigation through the integration of multi-sensor fusion is described in [24]. A SLAM algorithm relying on 3D LiDAR data, and thus more suitable for outdoor environments, such as vineyards, is presented in [25]. Furthermore, a feature-extraction method specifically designed for SLAM in vineyard is proposed in [16]. Moreover, in [26] a scan filter is implemented together with LiDAR SLAM to detect the motion status of objects in the vineyard, and to use the most stable ones as landmarks for robust robot localization. Differently from that approach, the mobile robot for arable farming described in [27] exploits a SLAM method based on a sequence of images captured in the field.

Commonly, mobile robots use 3D LiDAR SLAM algorithms not only for navigation, but also to reconstruct the 3D map of the vineyard, as the one used for canopy density estimation in [28]. However, the geometric information is not always sufficient to obtain insights on the vegetation status, and the spectral response of the canopy (how pigments absorb electromagnetic radiation) should also be considered to analyze plants health [19]. More in detail, the discrepancy in reflectance between the red and near-infrared (NIR) bands, and the spectral response in the transition zone (red edge), may provide crucial information on the state of the vegetation. For this purpose, special sensors and cameras, designed to capture specific wavelengths, can be integrated in mobile robots to compute vegetation indexes [29]. The spectral data acquired with those sensors are generally used for generating 2D maps of the field [18]. Examples of mobile robots capable of fusing geometric and multispectral data can be found in [17,30]. However, although these robots are able to extract a multitude of information, they lack autonomous navigation capabilities. Most of the mobile robots designed for vineyard mapping are steered manually from remote or are only capable of following a row exploiting reactive navigation techniques based on local perception of the field (e.g., based on ultrasound [19] or LiDAR data [20]), as it is reported in Table 1.

In the context of mobile robotics for applications in viticulture, open-source datasets gathered by mobile robots are essential for advancing autonomous navigation and mapping techniques, as they offer real-world data for developing, testing, and improving algorithms. In the last years, several publicly available datasets have been released to support the progress of these autonomous systems. Notable examples of agricultural dataset are the MAgro dataset [20] and the BLT dataset [12], collected by mobile robots equipped with LiDAR sensors, IMUs, GNSS-RTK receivers, and stereo cameras. Moreover, the ARD-VO dataset [18] shows that multispectral images collected by a mobile robot can be used to compute several vegetation indexes. Similarly, the CitrusFarm dataset [31] provides both multispectral and navigational sensor data collected in citrus tree fields. However, there is a paucity of datasets that include both data from onboard sensors and multispectral images collected in vineyards. These datasets are essential for advancing research in precision viticulture, particularly in areas such as autonomous navigation, environmental perception, and crop condition assessment.

To address this gap, in this work we introduce the FriûlBot open-source dataset specifically collected in vineyard settings. The dataset is designed to support and accelerate the development and benchmarking of algorithms for localization, mapping, and multi-sensor data fusion. The collection of data consists of both sensor measurements and multispectral images acquired in the field by the robot autonomously inspecting the vineyard rows. The mobile platform used to acquire the FriûlBot dataset is shown in Fig. 1.

Differently from other mobile robots designed for mapping in vineyards, the mobile robot presented in this work is capable of reconstructing a 3D map of the field that integrates both geometric and multispectral data, achieved through the fusion of information from a LiDAR sensor and a multispectral camera. The robot can navigate autonomously reaching pre-defined GNSS way points in a vineyard. The integrated path planning strategy is customized for mobile robots equipped with a camera directed to the plants (Fig. 3), thus making the robot traverse each vineyard corridor in both directions to capture

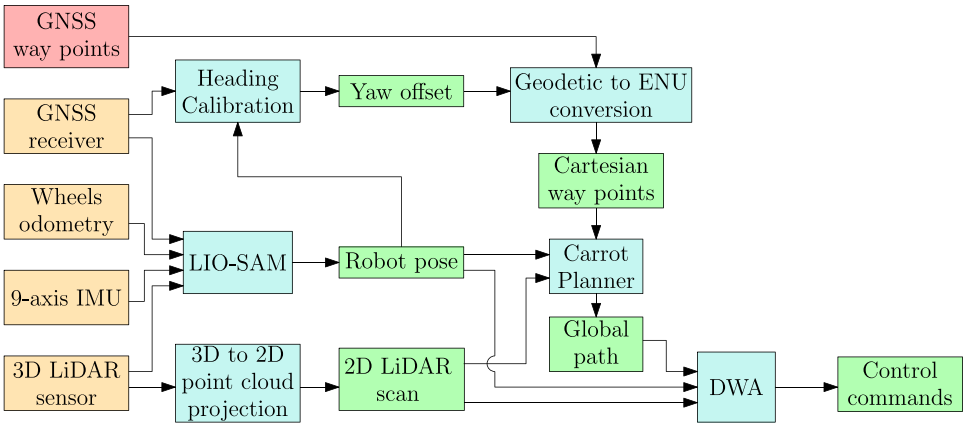

Fig. 2. Architecture of the proposed navigation approach. User inputs are reported in red, sensor data in orange, algorithms in light blue, and outputs in green.

data from both sides. The proposed approach is tested in a vineyard of the University of Udine (Friuli Venezia Giulia, Italy). The results of extensive experiments in the field demonstrate that the robot is able to navigate following long and repeatable paths that allow for consistent data collection and mapping. Furthermore, the autonomous mobile robot shows its ability in the reconstruction of point clouds of the vineyard that also display the values of different vegetation indexes.

The main contributions of the paper can be summarized as follows:

- an open-source dataset collected in vineyard and aimed at catalyzing the development of localization, mapping and multi-sensor fusion techniques;
- an autonomous navigation and mapping approach designed for mobile robots exploring vineyard rows;
- a strategy to fuse LiDAR data and multispectral images;
- the results of extensive experimental tests in a vineyard to demonstrate the performance of the autonomous navigation and mapping approach.

The proposed autonomous robotic system can be employed for vegetation monitoring over a long time frame (e.g., for disease detection, assessment of water stress, and evaluation of overall crop health), not only in vineyards, but also in orchards or other agricultural settings. Its capability for consistent and repeatable data acquisition over extended periods makes it particularly suitable for applications requiring temporal analysis of plant conditions. Nevertheless, the detailed investigation of case studies involving repeated monitoring campaigns or multi-seasonal analyses lies beyond the scope of the present work.

The paper is organized as follows: Section 2 describes the proposed strategy for autonomous navigation and multi-sensor fusion. The experimental setup is illustrated in Section 3, whereas the experimental results are presented in Section 4. Section 5 illustrates the open-source dataset collected by the robot in the field. Finally, Section 6 concludes the paper.

2. Navigation and mapping approach

In this paper we address the problem of the autonomous navigation of a mobile robot through vineyard rows while simultaneously collecting geometric and multispectral data. The proposed strategy requires only the GNSS coordinates at the beginning and at the end of the vineyard rows as user inputs to plan a safe path for the robot. The approach integrates data from the LiDAR sensor, IMU, GNSS, and wheels odometry, to build a 3D point cloud of the surrounding environment.

2.1. Autonomous navigation

An overview of the autonomous navigation framework proposed in this work is illustrated in Fig. 2. The approach is tailored for a robot navigating in vineyard, but it can be also applied to other types of orchards where plants are arranged in rows. The navigation method relies on GNSS way points in form of latitude and longitude coordinates in the World Geodetic System 1984 (WGS 84) and orientation of the robot with respect to the magnetic North as user inputs. A list of GNSS way points indicating the positions in which the robot has to enter and exit the vineyard rows has to be provided at the beginning of the survey. We assume that the robot is moving on a plane. The GNSS way points, initially in geodetic decimal degrees coordinates, are than expressed with respect to the local East-North-Up (ENU) reference frame (Cartesian coordinates) before being exploited for path planning.

The autonomous navigation framework is designed for a mobile robot with a multispectral camera mounted on one side that points to the plants (Fig. 3). In this configuration, the camera can only capture one side of the vineyard corridor at a time (e.g., the plants on the right if the camera is mounted on the right side of the robot). To cover both sides, the robot should drive back and forth along each corridor of the vineyard. For this reason, additional way points are automatically computed at the end of each corridor to allow the robot to turn around and go back, as it is shown in Fig. 3. The decision to use a single multispectral camera was primarily driven by cost considerations and the goal of simplifying the sensor setup and synchronization process. Employing only one camera reduces the overall system complexity, minimizing potential calibration and synchronization issues between multiple sensors, while still allowing to capture comprehensive canopy data by traversing each row twice. However, the proposed navigation and mapping approach is fully scalable and can be easily extended to configurations with two cameras, if available. In this case, the navigation process would be further simplified, as the robotic system could simultaneously capture both sides of the row, thus requiring only a single traversal per vineyard corridor.

Since the middle of the corridors are considered free from obstacles, the desired path is planned using straight lines connecting the way points under the assumption that the robot is navigating in a simplified 2D plane, despite the complexities of the real-world environment. For this purpose, the Carrot Planner [32] is used as global path planner. The Carrot Planner takes a goal point as input from the external user, checks if the user-specified goal is in an obstacle, and if it is, it walks back along the vector between the user-specified goal and the mobile robot until a goal point that is not in an obstacle is found. It then passes this target point on as a plan to the local planner of the robot. In this way, the Carrot Planner plans the overall route using straight paths that connect each pair of consecutive way points, and allows the robot to get as close to each user-specified way point as possible.

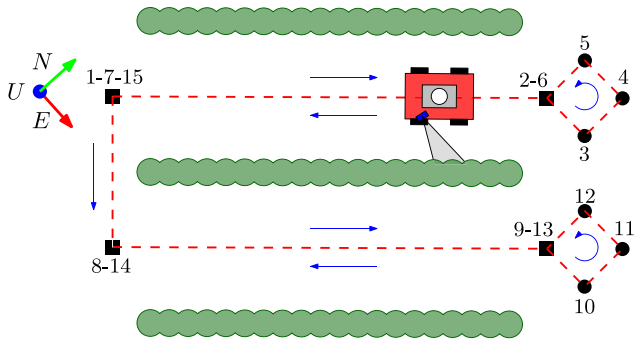

Fig. 3. Path planning in the vineyard. Black squares indicate the GNSS way points provided as user inputs. The additional way points that are automatically generated are marked with black dots. The numbers indicate the order in which the robot reaches the way points. The field of view of the camera pointing to the plants is depicted in gray.

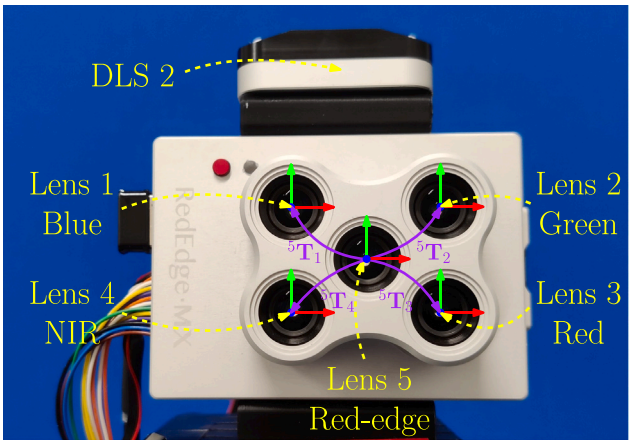

Fig. 4. Micasense RedEdge-MX multispectral camera and Downwelling Light Sensor (DLS 2). The ID of the lenses are reported in yellow together with the corresponding spectral bands. The relative transformations between each lens and the reference one are depicted with purple arrows.

Furthermore, the Dynamic Window Approach (DWA) algorithm [33] serves as local path planner. In case of unexpected static or dynamic obstacles on the robot path, the DWA algorithm modifies on-the-fly the global path to avoid potential collisions while balancing safety and proximity to the way point. Both path planners use costmaps (i.e., 2D maps where each cell is assigned a cost value, indicating the difficulty or risk of traversing that area) that are retrieved by using the most recent 2D LiDAR scan acquired by the robot. The 2D LiDAR scan is obtained from the 3D LiDAR data by projecting the point cloud in the plane in which the path is planned. Using the projected 3D LiDAR scan allows the robot to consider the geometry of the objects in the field and avoid potential obstacles.

To follow the planned path, the robot requires an estimate of its current pose in the vineyard. The localization relies on data from a GNSS receiver, an IMU sensor, wheels encoders, and a 3D LiDAR sensor. The LiDAR SLAM algorithm LIO-SAM [34] is used to fuse the data from each source and to provide a solution for the localization of the mobile robot as a 6-DOF pose. To this aim, the 3D point cloud of the environment is continuously updated and employed to perform the scan-matching operation using LiDAR data that are downsampled with a voxel filter. Furthermore, a threshold based on the traveled distance of the robot is used to trigger the update of the map with a new 3D LiDAR scan. LIO-SAM initializes the ENU reference frame exploited for the autonomous navigation and mapping by using the readings from the IMU. Both GNSS measurements and a loop closure strategy are used by LIO-SAM to correct the accumulated drift. This SLAM algorithm has been chosen since the integrated strategies to correct the accumulated drift make it suitable for long outdoor surveys. Moreover, it demonstrates to be a good compromise between accuracy and density of the 3D reconstruction compared to alternative approaches [35]. In that paper, a regular and structured environment was selected to evaluate the mapping performance of the robotic system in a controlled scenario, with respect to a ground truth acquired with a high-precision topographic instrument. The work in [35] was preliminary for the application of the robotic system in an unstructured agricultural context, presented in this manuscript.

Before converting the GNSS way points to ENU Cartesian coordinates, a specific heading calibration procedure is used in the navigation framework to estimate the bias between the magnetic North and the true North (the direction towards the geographic North Pole). This bias is caused by the presence of ferromagnetic objects, currents, and by the magnetic declination of the Earth. The procedure for the heading calibration is the following. First, the ENU reference frame is initialized by the SLAM algorithm. Then, the mobile robot is commanded to follow a straight path while collecting a set of GNSS measurements together with the corresponding position of the mobile robot provided by the SLAM algorithm. Subsequently, a conversion is applied to the set of GNSS measurements changing the coordinates from WGS84 geodetic to Cartesian coordinates expressed with respect to the ENU* reference frame, which has its origin and U-axis coincident with those of ENU and its N-axis pointing to the geographic North Pole. This operation results in two set of points whose coordinates differ from each other only by a rotation in the plane orthogonal to the U-axis. The set of coordinates in ENU* is denoted with **P**, whereas the set in ENU with **Q** (both **P** and **Q** are $3 \times n$ matrices, with n the number of points in each set). Since the correspondences between the points of the two sets are known, the rotation matrix **R** that aligns **P** with **Q** can be calculated directly using the SVD decomposition [36] of the cross-covariance matrix **K** of **P** and **Q** as follows:

$$\text{SVD}(\mathbf{K}) = \mathbf{USV}^T \quad \Rightarrow \quad \mathbf{R} = \mathbf{UV}^T, \tag{1}$$

with **U** and **V** orthogonal matrices whose columns are the left-singular and right-singular vectors of **K**, respectively. **S** is a diagonal matrix containing the singular values of **K**. The matrix **R** only depends on the angle between the E-axis of ENU and ENU* reference frames. Given the estimated bias, described by **R**, the GNSS way points can be transformed in Cartesian way points expressed in the local ENU reference frame and used for path planning.

2.2. LiDAR and multispectral data fusion

To merge the 3D point cloud obtained from the SLAM algorithm with the information on the vegetation indexes, the data from the LiDAR sensor have to be coupled with those of the multispectral camera. This operation requires: (i) the intrinsic calibration of all the m lenses of the multispectral camera; (ii) the extrinsic calibration between the $m-1$ lenses of the multispectral camera and a designated reference lens; (iii) the extrinsic calibration between the reference lens and the LiDAR sensor; (iv) the radiometric calibration of each raw multispectral image; (v) the projection of the 3D LiDAR scans on the calibrated images to associate radiometric information to the point clouds.

The intrinsic calibration (i.e., the estimation of the focal length, the principal point, and the lens distortion coefficients) of the multispectral camera is required, before each experimental campaign, to correct the estimation of the interior orientation parameters that might change over time due to vibrations and temperature. This calibration is performed with a squared checkerboard. The aspect ratio is enforced to be fixed and an 8-parameters model agnostic on the geometry of the lens is used for the distortions [37].

The extrinsic calibration of the lenses provides the transformation matrices ${}^{k}\mathbf{T}_i$ ($i \in \{1, 2, \dots, m\} \mid i \neq k$, with i denoting the lens that captures the image) describing the pose of the lenses with respect to the reference lens [38], as shown in Fig. 4. The relative orientation and position of each couple of lenses is estimated with the same checkerboard used for the intrinsic calibration.

Moreover, an extrinsic calibration between the LiDAR sensor and the designated reference lens of the camera is required to fuse the data from the two sensors. This calibration provides the transformation matrix ${}^{\mathrm{L}}\mathbf{T}_k$ describing the pose of the reference lens with respect to the LiDAR sensor reference frame. The calibration is performed as follows. First, the SLAM algorithm is started with the fixed reference frame in the initial pose of the LiDAR sensor. While the robot remains stationary, the images are captured by orienting the camera toward two non-parallel plane panels. The robot is then moved closer to and farther from the panels to fully capture their geometry using the LiDAR sensor. Instead of using a single, sparse scan, the SLAM algorithm provides a point cloud that is utilized in the calibration process to ensure its applicability to low-resolution LiDAR sensors. The calibration is formulated as a Perspective-n-Point (PnP) problem, i.e., finding the camera pose given the 3D points at the corners of the panels in the point cloud and the corresponding projections on the image, as well as the intrinsic parameters of the lens. A robust solution to the PnP problem is obtained by applying the RANSAC algorithm to remove outliers. Finally, the calibration is refined by iteratively minimizing the reprojection error using the Levenberg–Marquardt method.

The radiometric calibration of the multispectral camera is carried out to obtain the reflectance measurements that are needed to compute the vegetation indexes. The radiometric calibration accounts for the responses of the sensor to varying lighting conditions and enables a consistent data collection along the vineyard rows and across multiple epochs. The radiometric calibration aims at converting raw pixel values to reflectance data. Since the lighting conditions among vineyard rows may vary over time, the radiometric calibration is performed using metadata acquired by a specific light sensor related to each single capture. First, the raw pixel data are converted in calibrated radiance images. The raw images are normalized by the image bit depth and the vignette effect (i.e., the decrease in light sensitivity that occurs in pixels farther from the center of the pixel array) is corrected as described in [39]. After this operation, the reflectance images $\mathcal{R}_i$ are computed as:

$$\mathcal{R}_i(x, y) = \frac{\pi \mathcal{L}_i(x, y)}{I_i}, \quad i = 1, 2, \dots, m \tag{2}$$

where $\mathcal{L}_i(x, y)$ is the value of the radiance of the pixel in position (x, y), whereas I_i is the value of the irradiance of the sun for a specific light band.

To associate radiometric data to the 3D LiDAR scans, the point clouds ${}^{\mathrm{L}}\mathbf{P}$ (Cartesian coordinates expressed in homogeneous coordinates with respect to the sensor reference frame L) are projected on the reflectance images, which are acquired at a lower frequency than the LiDAR data. To exploit every 3D LiDAR scan acquired between two consecutive multispectral images, the 3D LiDAR scans are expressed with respect to the reference frame L^*, i.e., the reference frame of the LiDAR sensor at the time of the most recent captured multispectral image. More in detail, the pose of the LiDAR sensor is known, from the SLAM algorithm, with respect to the fixed ENU reference frame used for the navigation every time the LiDAR sensor acquires a scan ${}^{\mathrm{L}}\mathbf{P}$, and is given by the transformation matrix ${}^{\mathrm{ENU}}\mathbf{T}_{\mathrm{L}}$. The pose of the LiDAR sensor during the last camera capture is given by the transformation matrix ${}^{\mathrm{ENU}}\mathbf{T}_{\mathrm{L}^*}$ (at each capture ${}^{\mathrm{ENU}}\mathbf{T}_{\mathrm{L}}$ updates ${}^{\mathrm{ENU}}\mathbf{T}_{\mathrm{L}^*}$). Therefore, each 3D LiDAR scan ${}^{\mathrm{L}}\mathbf{P}$ can be expressed with respect to the reference frame L^* with:

$${}^{\mathrm{L}^*}\mathbf{P} = ({}^{\mathrm{ENU}}\mathbf{T}_{\mathrm{L}^*})^{-1}\ {}^{\mathrm{ENU}}\mathbf{T}_{\mathrm{L}}\ {}^{\mathrm{L}}\mathbf{P} \tag{3}$$

Finally, the parameters estimated with the intrinsic and extrinsic calibrations are used to project the 3D LiDAR scans ${}^{\mathrm{L}^*}\mathbf{P}$ on the reflectance images $\mathcal{R}_i$ involved in the computation of the considered vegetation index, e.g., the red band and the NIR image for the Normalized Difference Vegetation Index (NDVI). The reflectance value of the pixel on which each point is projected is assigned to the corresponding point in the 3D LiDAR scan. However, the LiDAR points within the field of view (FoV) of one lens may not be within the FoV of the other lens, and vice versa. For this reason, only points in both FoVs are used to compute the considered vegetation index.

3. Experimental setup

The proposed approach for autonomous navigation and mapping in vineyards is tested using an AgileX Scout 2.0 mobile robot, shown in Fig. 1. The Scout 2.0 is a wheeled skid-steered ground robot suitable for outdoor applications in rough terrains. The mobile robot is equipped with a NVIDIA Xavier computer running Ubuntu 18.04 with ROS Melodic and a custom sensor suite. The implementations of the Carrot Planner and the DWA algorithm available in the navigation package of ROS Melodic are used for path planning. The sensor suite features a Velodyne VLP-16 LiDAR sensor, an Xsens MTi-630 9-axis IMU, an Ardusimple simpleRTK2B Budget kit for GNSS measurements, and a Micasense RedEdge-MX multispectral camera. The specifications of the devices onboard the robot are reported in Table 2.

The LiDAR sensor is mounted horizontally on the robot chassis with the IMU sensor and the GNSS antenna mounted on top of it thanks to a 3D printed support. The multispectral camera is positioned to the right side of the robot and oriented to face the plants. An LTE router is also integrated in the robot providing Internet connection to the onboard computer.

The Velodyne sensor is connected to the computer via Ethernet and the data transmission is conducted via UDP protocol using the Velodyne ROS drivers. The IMU consists of a magnetometer, a gyroscope, and an accelerometer. The direct measurements of these sensors are processed using an integrated Kalman filter, which fuses the IMU data to deliver the orientation of the sensor relative to the magnetic North, the linear accelerations, and the angular velocities at a rate of 200 Hz.

The GNSS is based on a single U-blox F9P receiver, and it is provided with differential corrections to achieve an RTK-FIX solution using an Networked Transport of RTCM via Internet Protocol (NTRIP) service. The HxGN SmartNet is used as the NTRIP service obtaining an horizontal accuracy estimated by the receiver below 2 cm. The ROS integration is implemented using the ublox_utils ROS package.

The Micasense RedEdge-MX is a multi-lens multispectral camera (Fig. 4) that captures five bands from separate lenses: three in the visible portion of the light spectrum (red, green, and blue), and two in the invisible portion (red edge and near-infrared). The intrinsic and extrinsic calibration of the camera is performed by using OpenCV built-in functions. The Downwelling Light Sensor (DLS 2) is directly connected to the Micasense camera, mounted on top of the camera and pointing towards the sky. The DLS 2 measures the ambient light (i.e., incoming spectral irradiance) and sun angle for each of the five bands of the camera and records this information in the metadata of the TIFF images captured by the camera.

4. Experimental results

The experiments are conducted in the vineyard of the University of Udine (Friuli Venezia Giulia region, Northeastern Italy). The plants in the vineyard are arranged with a spacing of 1.0 meter between individual plants and 2.5 m between rows, each of which is approximately 100 m long. Three experiments are conducted under full daylight conditions, between July 22 and July 25, 2024. In the first experiment (Test 1) the mobile robot navigates in a single row, whereas in the second (Test 2) and third (Test 3) the robot surveys three and five rows, respectively.

Table 2
Specifications of the onboard devices of the robot.

Device	Manufacturer	Model	Specifications
Mobile robot	AgileX	Scout 2.0	Weight: 62 Kg; length: 930 mm; width: 699 mm; height: 348 mm; motor: DC brushless 4X 200 W; reduction gearbox: 1:30.
Computer	NVIDIA	Jetson AGX Xavier	GPU: 512-core NVIDIA Volta architecture, 64 Tensor Cores; GPU max frequency: 1377 MHz; CPU: 8-core NVIDIA Carmel Arm v8.2 64-bit CPU 8 MB L2 + 4 MB L3; CPU max frequency: 2.2 GHz; OS: Ubuntu 18.04; ROS Melodic.
LiDAR sensor	Velodyne	VLP-16	Channels: 16; measurement range: 100 m; range accuracy: up to ±3 cm; FoV (vertical): ±15° (30°); angular resolution (vertical): 2°; FoV (horizontal): 360°; angular resolution (horizontal/azimuth): 0.1° ÷ 0.4°; rotation rate: 5 Hz ÷ 20 Hz.
IMU	Xsens	MTi-630	Sensor fusion accuracy: 0.2° roll/pitch, 1° heading: gyroscope noise density: 0.007 °/s/$\sqrt{\text{Hz}}$; accelerometer noise density: 60 μg/$\sqrt{\text{Hz}}$.
GNSS receiver	U-blox	ZED-F9P	Precision: ≤1 cm with NTRIP; update rate: max. 10 Hz; first RTK fix: 35 s; raw data output: UBX format.
Multispectral camera	Micasense	RedEdge-MX	Pixel size 3.75 μm; aspect ratio 4 : 3; FoV 47.2° (horizontal), 35.4° (vertical); resolution 1280 × 960 (1.2 MP × 5 images); output bit depth: 12-bit; center wavelengths: 475 nm (blue), 560 nm (green), 668 nm (red), 717 nm (red-edge), 842 nm (near-infrared).

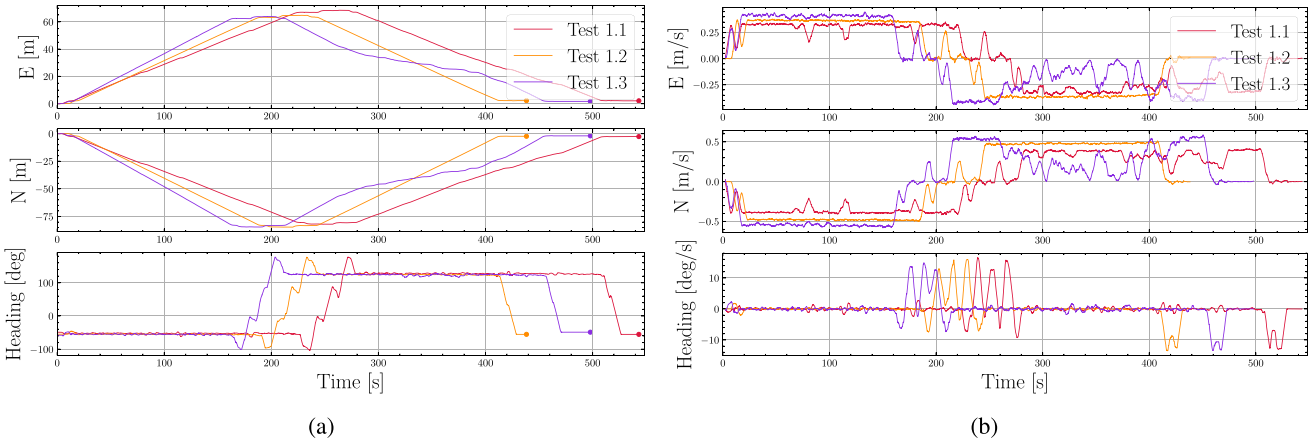

Fig. 5. Mobile robot trajectories in Test 1: (a) positions and (b) velocities over time.

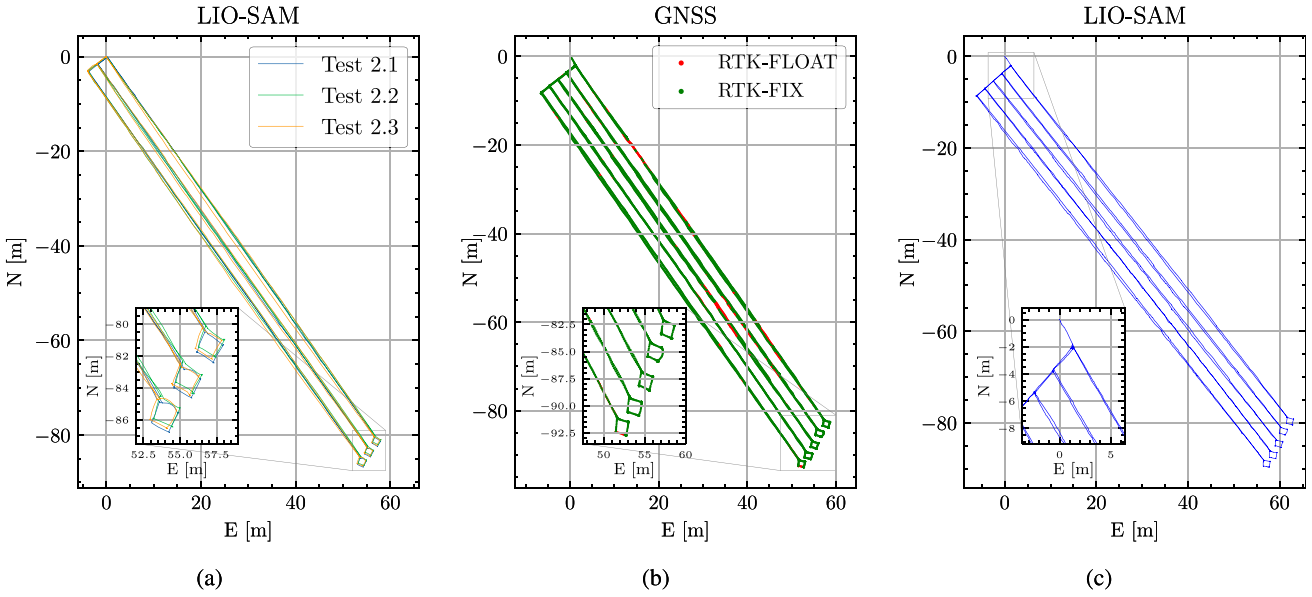

Fig. 6. Plot of the paths of the robot during autonomous navigation: (a) paths tracked by LIO-SAM in navigating among three rows in Test 2; (b) path tracked by the GNSS measurements in Test 3; and (c) by LIO-SAM in Test 3.

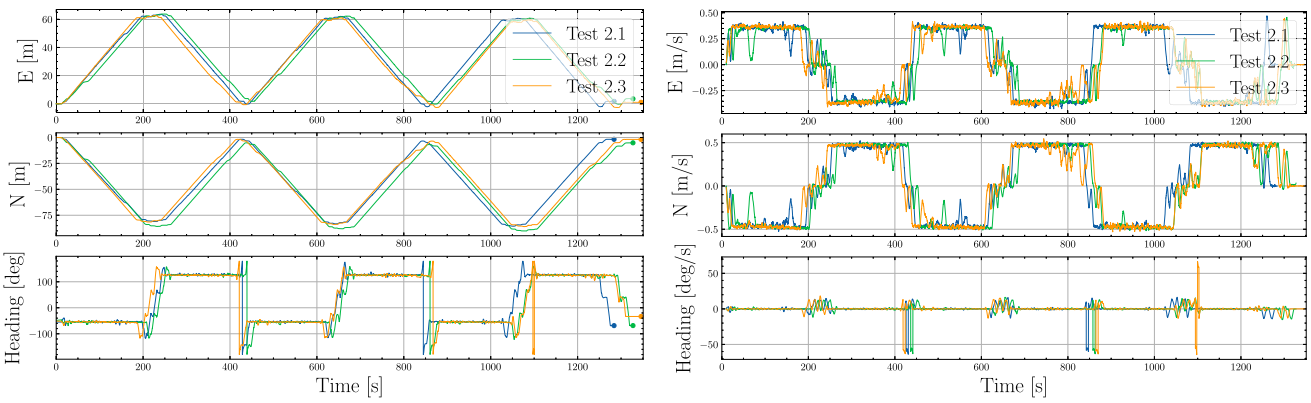

(a) (b)

Fig. 7. Mobile robot trajectories from repeated runs in Test 2: (a) positions and (b) velocities over time.

Table 3
Experimental results of Test 1.

Trial	Max. speed [m/s]	Path length [m]	Path duration [s]	Avg. speed [m/s]	Point density [pts/m^2]
Test 1.1	0.6	229.0	513	0.45	4351
Test 1.2	0.7	224.2	410	0.55	7253
Test 1.3	0.8	236.5	457	0.52	6241

4.1. Autonomous navigation

The first experimental test (Test 1) is carried out to determine the optimal value for the maximum translational speed of the controller that generates the commands for steering the robot through the vineyard rows. Three trials (Test 1.1, Test 1.2, and Test 1.3) are carried out in a single row of the vineyard using the same GNSS way points as user inputs. The maximum speed is progressively increased in each attempt, ranging from 0.6 to 0.8 m/s, with an incremental step of 0.1 m/s. The results of Test 1 are reported in Table 3. In the first and second trials (Test 1.1 and 1.2), the autonomous robot successfully completes the survey avoiding obstacles (i.e., branches extending into the center of the row). On the other hand, the excessive maximum speed set for the third attempt (Test 1.3) causes the failure in avoiding the branches resulting in the robot getting stuck for a while. Therefore, subsequent experiments are conducted with the maximum speed set to 0.7 m/s. The robot positions and velocities over time for each trial are shown in Fig. 5. Notably, during Test 1.3, an anomalous behavior can be observed, as the obstacle encountered in the second part of the survey caused irregularities in both position and speed profiles.

In Test 2, the robot conducts repeated surveys (Test 2.1, Test 2.2, and Test 2.3) of three vineyard rows. Each survey is performed on a different day, with the navigation framework reinitialized for each attempt while maintaining the same GNSS waypoints as user inputs. The GNSS receiver provides a solution of type RTK-FIX only in 85.5%, 86.3%, and 59.2% of the survey in Test 2.1, Test 2.2, and Test 2.3, respectively. Despite this, the robot successfully follows the planned path and reaches the way points due to the integrated localization approach. During the three trials of Test 2, the robot navigates an average path length of 626.8 meters, with a standard deviation of 33 cm. The average total duration of the survey is 21 minutes and 36 seconds, with a standard deviation of 25 seconds. The paths estimated by LIO-SAM in each trial of Test 2 are illustrated in Fig. 6(a), while Fig. 7 shows the East, North, and Heading components of the robot position and velocity recorded during Test 2. The three repetitions exhibit highly consistent and closely overlapping trends.

The repeatability of the paths of Test 2 is also analyzed by using the Hausdorff distance, i.e., the maximum distance between any point in one set and the nearest point in the other one. The Hausdorff distance is computed for each combination of paths obtained in Test 2. An Hausdorff distance of 52.8 cm is obtained between Test 2.1 and Test 2.2, of 78.9 cm between Test 2.1 and Test 2.3, and of 85.2 cm between Test 2.2 and Test 2.3. On average, the Hausdorff distance between the paths is 72.3 cm, with a standard deviation of 14.0 cm. A lower Hausdorff distance between the paths could be obtained by incorporating intermediate way points along the vineyard rows. However, the robot successfully navigates autonomously using only the starting and ending points of the rows.

To assess the potential drift in the localization during Test 2, we calculate the Euclidean distance between the position of the robot upon reaching the first way point and its position upon returning to the same way point at the conclusion of the survey using GNSS readings. The distance between the first way point and the final position of the robot is 21.4 cm for Test 2.1, 15.9 cm for Test 2.2, and 20.4 cm for Test 2.3.

Test 3 involves an extensive mapping of five vineyard rows, to evaluate the robustness of the navigation approach in a longer survey. The path followed by the robot during this final test is illustrated in Figs. 6(b), and 6(c). In Test 3, the GNSS receiver is able to provide a solution of type RTK-FIX in the 91% of the duration of the survey. Nonetheless, the SLAM algorithm guarantees a reliable localization during the whole duration of the survey. The robot navigates autonomously for a total distance of 1052.3 meters and for approximately 37 minutes, and, at the end of the test, it successfully returns to the starting point with a position error of only 13.3 cm.

With the proposed navigation framework, the mobile robot demonstrates to be able to provide repeatable paths that allow for a consistent data collection. Moreover, the approach proves robust in long surveys even in case of inaccurate GNSS measurements (Fig. 6(b)).

4.2. Mapping

The intrinsic and extrinsic calibrations of the lenses of the multispectral camera are conducted using 40 images of a checkerboard panel having 6 rows and 8 columns, with each square measuring 2.85 cm. The reprojection error of the intrinsic calibration of the lenses, defined as the arithmetic mean of the errors calculated for all the 40 images, is equal to 0.03 pixels. The red-edge lens is selected as the reference lens since it is centrally placed in the camera (Fig. 4). The results of the extrinsic calibration between the red-edge lens and the other lenses of the multispectral camera are shown in Fig. 8(a). Furthermore, the pose of the red-edge lens with respect to the LiDAR sensor reference frame is illustrated in Fig. 8(b).

The multispectral images are collected in each survey of Test 2 and Test 3, and used to compute three different vegetation indexes: the NDVI, the Normalized Difference Red-Edge (NDRE), and the Green

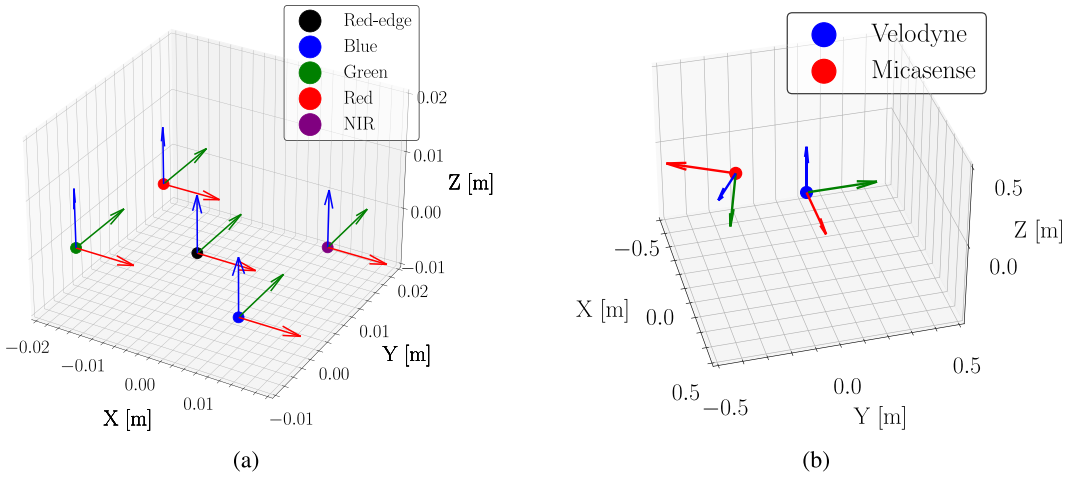

Fig. 8. (a) Positions and orientations of the blue, green, red, and NIR lenses with respect to the red-edge lens. (b) Position and orientation of the red-edge lens with respect to the LiDAR sensor. The red arrow represents the X-axis, the green arrow the Y-axis, and the blue arrow the Z-axis.

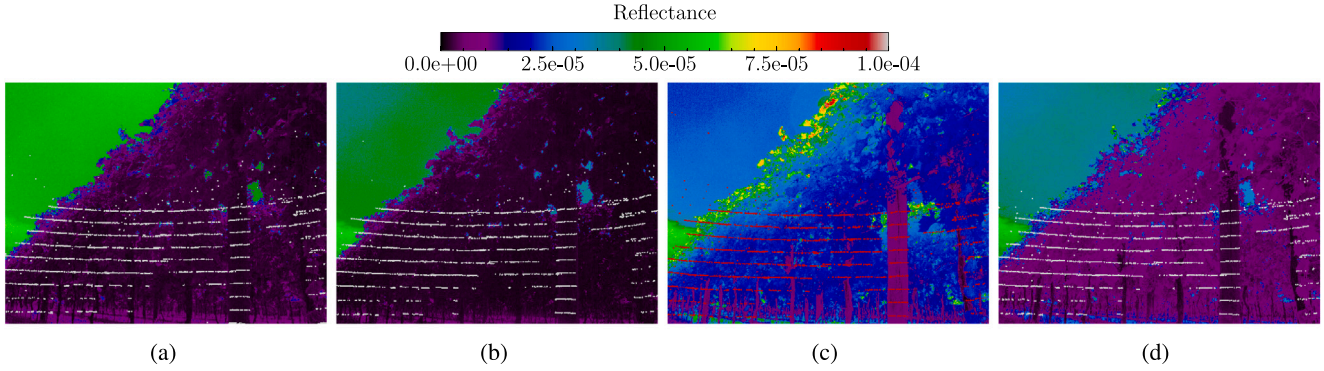

Fig. 9. 3D LiDAR scans projected on the reflectance images of (a) the green, (b) the red, (c) the NIR, and (d) the red-edge lenses.

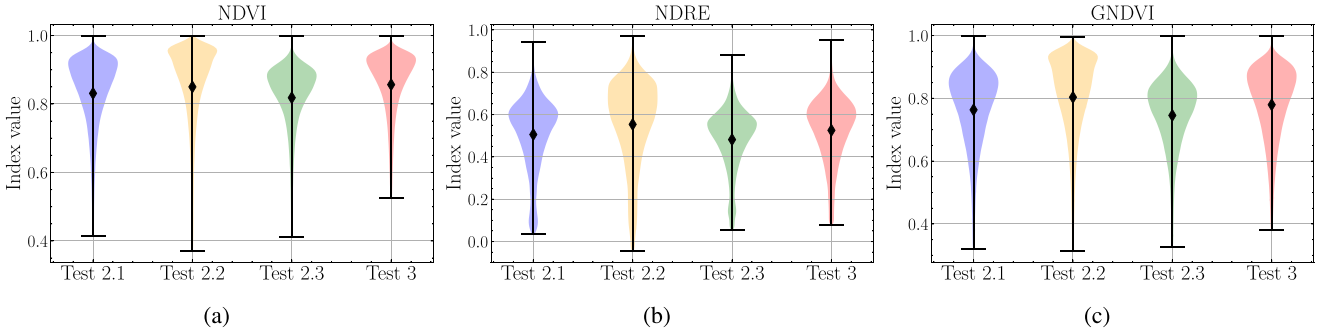

Fig. 10. Violin plots of the vegetation indexes in the point clouds of Test 2 and Test 3: (a) NDVI, (b) NDRE, (c) GNDVI. The black markers indicate the mean values of the vegetation indexes, whereas the whiskers extend to the most extreme data points not considered outliers.

NDVI (GNDVI). These vegetation indexes involves the green, the red, the red-edge, and the NIR spectra of the light, and are computed as follows: NDVI = (NIR−Red)/(NIR+Red), GNDVI = (NIR−Green)/(NIR+Green), and NDRE = (NIR − Red-edge)/(NIR + Red-edge).

NDVI values span from −1.0 to 1.0, where negative values are associated with non-vegetative surfaces such as clouds or water, and high positive values indicate the presence of vegetation. Low values (from 0.0 to 0.6) correspond to sparse or stressed vegetation, whereas values above 0.6 represent dense and vigorously growing vegetation. However, the NDVI is suitable to analyze the vigor of plants at an early stage of growth, whereas in more advanced stages of development, the GNDVI provides a higher saturation point. Moreover, the NDRE can be used in case of dense canopies to detect changes in the chlorophyll content. To compute the considered vegetation indexes, whose values are then appended to the point cloud, each 3D LiDAR scan is projected on the reflectance images captured by the green, red, red-edge, and NIR lenses, as it is illustrated in Fig. 9.

The distributions of the values of the vegetation indexes calculated for each trial of Test 2 and Test 3 are shown using violin plots in Fig. 10. In these plots, the outliers are removed with the interquartile range method to better visualize the data. The largest difference between the mean values of the vegetation index is 0.07 recorded for the NDRE between Test 2.2 and Test 2.3. Since the data are collected on consecutive days, no significant changes in the status of the vegetation are expected. Therefore, the minimal variation observed between the tests confirms the repeatability of the approach.

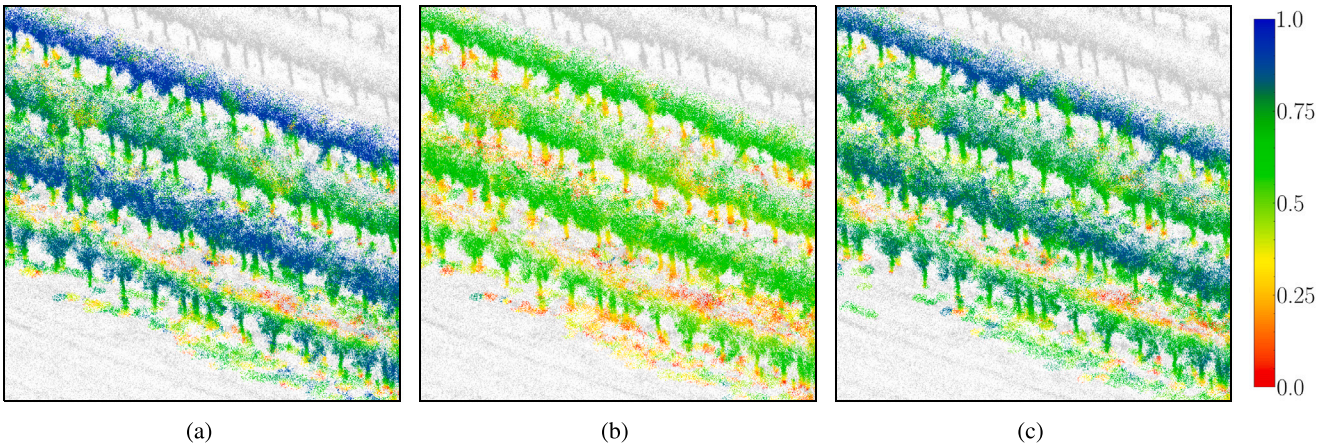

Fig. 11. Point clouds of the three vineyard rows of Test 2 colored with (a) the NDVI, (b) the NDRE, and (c) the GNDVI vegetation indexes.

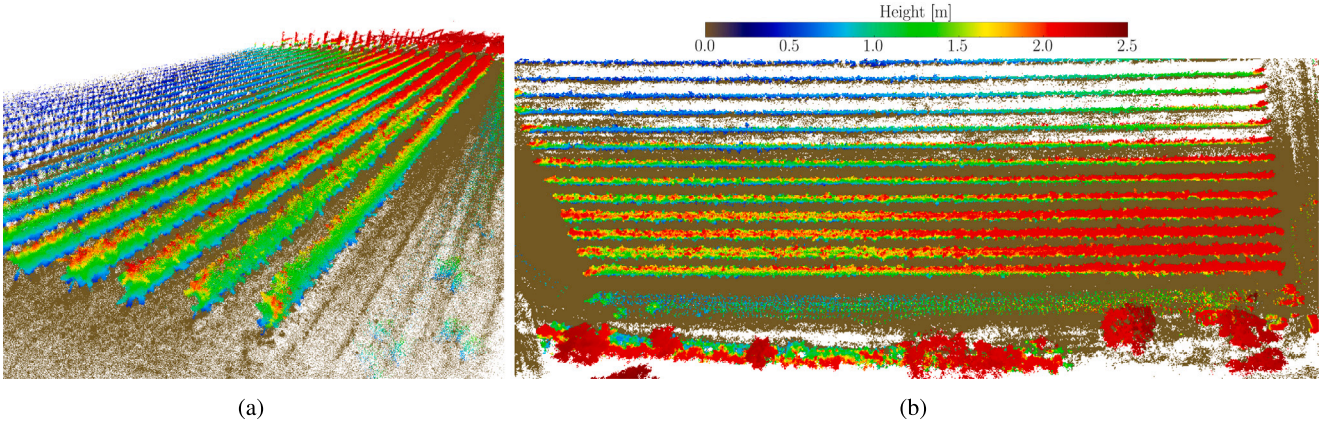

Fig. 12. Point cloud of the vineyard rows acquired during Test 3, with colors representing the height of the plants in meters: (a) 3D view, (b) top view.

The 3D LiDAR scans enhanced with vegetation indexes are post-processed together with the data from all the other odometry sources using LIO-SAM to reconstruct the maps of the vineyard rows. The point clouds with the NDVI, NDRE, and GNDVI vegetation indexes obtained in Test 2.1 are shown in Figs. 11(a), 11(b), and 11(c), respectively.

Since the FoV of the multispectral camera is narrower compared to that of the LiDAR sensor, only a limited number of points in the map of the vineyard are associated with a vegetation index, e.g., 5% of the points in the point clouds of Test 3. For this reason, the point clouds in Fig. 11 are post-processed to enhance the visualization of the indexes values. More in detail, at each point in the map without a vegetation index is assigned the average value of the vegetation indexes from the nearest points within a 20 cm radius. This threshold was manually tuned during the preliminary post-processing of the data. If a point lacks any neighboring points with a vegetation index within this 20 cm radius, it remains unassociated with a vegetation index. The points with a low vegetation index value in the map (Fig. 11) are marked in red, with values increasing through yellow and green, and the highest values are depicted in blue. Moreover, the point clouds obtained in Test 3 are shown in Fig. 12, where the points belonging to the ground are represented in brown, and the colormap indicates the height of the plants.

In conclusion, the proposed approach successfully integrates LiDAR and multispectral data to generate point clouds of the vineyard with vegetation indexes associated to each point, enabling spatial analysis for vineyard monitoring.

5. The FriûlBot open-source dataset

In this section, we describe the FriûlBot open-source dataset, collected to provide a reference testbed for the development and benchmarking of localization, mapping, and multi-sensor data fusion algorithms. The dataset, acquired during the experimental campaign conducted between July 22 and July 25, 2024, consists of raw ROS bag files and multispectral images collected in the field with the robot autonomously inspecting the vineyard rows, and it is accessible at the following link: https://github.com/diegotiozzo21/FRIULBOT_DATASET. The dataset includes information on the robot status, IMU, GNSS, and wheels odometry data, point clouds of the vineyard, and multispectral images. All the topics stored in the ROS bag files are described in Table 4. In order to access the data contained in the bag files, a dedicated Python processing script is available in the online repository.

The dataset comprises a file indicating the pose of each sensor with respect to the LiDAR sensor. The multispectral images are stored as TIFF files in separate directories for each survey. The data from the DLS2 light sensor are available as the metadata associated to each TIFF image of the multispectral camera. Additionally, the dataset includes the post-processed ROS bag files in which data from the LiDAR sensor and the Micasense camera are merged together to compute the vegetation indexes. The variable micasense_capture_lidar_points refers to the raw LiDAR scans that are temporally synchronized with the images captured by the multispectral camera (the multispectral camera operates at 0.5 Hz, while the LiDAR sensor publishes data at 10 Hz). Specifically, the triggering event of the multispectral camera also initiates the publication of micasense_capture_lidar_points, ensuring that

Table 4
Topics stored in each ROS bag file.

Topic	Message type	Rate [Hz]	Description
velodyne_points	PointCloud2	10	LiDAR scans of the Velodyne sensor.
imu/data	Imu	200	Linear accelerations, angular velocities, and orientation of the IMU.
ublox_position_receiver/fix	NavSatFix	3	GNSS measurements.
odom	Odometry	50	Odometry from the encoders of the wheels.
scout_status	ScoutStatus	50	Driver voltage and temperature, motor currents, velocities [rpm], and temperatures, battery current, voltage, temperature, state of charge (SOC), and state of health (SOH).
micasense_capture_lidar_points	PointCloud2	0.5	3D LiDAR scans captured synchronously with the image acquisition by the Micasense camera.
map_base_link/odometry	Odometry	20	Pose of the robot tracked by the SLAM algorithm.
tf	tfMessage	400	Transformations (translations and rotations) between different coordinate frames in the robot.

each LiDAR scan shares the same timestamp as the corresponding set of multispectral images, supporting reliable sensor fusion. Consequently, the number of LiDAR scans published under this topic is equal to the number of multispectral image captures (TIFF files). It is important to note that these data represent standard LiDAR point clouds, without any vegetation masks or spectral information. The fusion between LiDAR and multispectral data, as well as the computation of vegetation indexes, is performed exclusively during post-processing and not at the acquisition stage.

To add value and strengthen the utility of the dataset, a reproducible version of the autonomous navigation pipeline has also been published in the open-source repository. More in detail, all the configuration parameter files and the various launch files required to bring up all the autonomous navigation nodes, including those that are already available in other repositories (the dependencies of our framework) can be found in the online archive. Furthermore, a graph illustrating the structure of all nodes within the proposed framework can be found in the repository.

This dataset serves as a comprehensive resource aimed at fostering advancements in autonomous navigation, SLAM, and precision agriculture. It provides both raw and post-processed data, enabling researchers and developers to analyze sensor performance, validate algorithms, and benchmark their methods in realistic field conditions.

6. Conclusions

In this paper, we presented the FriûlBot open-source dataset, collected by an autonomous mobile robot for the 3D mapping and monitoring of vineyard environments. The proposed dataset constitutes a valuable contribution toward research on autonomous robotic systems operating in agricultural environments. By combining information from multiple onboard sensors, including geometric and multispectral data, it provides a solid experimental testing framework for the validation and comparison of localization, mapping, and sensor fusion approaches. This open-access resource is expected to support future developments in robotic perception, autonomous navigation, and precision agriculture applications.

The mobile robot designed to collect the FriûlBot dataset is capable of autonomously navigate vineyard rows while fusing data from a multispectral camera and a LiDAR sensor to map and monitor the field. To this scope, specific sensor calibrations have been introduced to define the relative pose of the sensors, correct the interference of the external magnetic fields on the IMU, and obtain radiometrically calibrated multispectral images. The proposed approach was extensively validated in the vineyard of the University of Udine, where the mobile robot autonomously reached GNSS way points navigating over a distance of one kilometer thanks to the integrated localization approach that exploits multiple odometry sources concurrently. The results confirmed the effectiveness of the robot in navigation, data collection, and mapping even in situation in which the GNSS receiver was not able to provide an accurate solution. By integrating the NDVI, the GNDVI, and the NDRE vegetation indexes, the robot built 3D point clouds enriched with information on the status of the plants.

Future work will focus on optimizing navigation in terrains with varying slopes and enhancing the obstacle avoidance strategy by incorporating data from multiple cameras. Moreover, loop closure strategies based on artificial intelligence [40] will also be introduced to further reduce drift. We also plan to extend the functionality of the robot by integrating a robotic arm for close-range measurements on the plants. Finally, the dataset presented in this work will be extended by adding repeated monitoring campaigns and multi-seasonal data acquisitions.

CRediT authorship contribution statement

Diego Tiozzo Fasiolo: Writing – original draft, Software, Resources, Investigation, Formal analysis, Data curation. **Lorenzo Scalera:** Writing – review & editing, Supervision, Resources, Methodology, Investigation, Formal analysis, Data curation, Conceptualization. **Eleonora Maset:** Writing – review & editing, Resources, Methodology, Investigation, Formal analysis, Data curation, Conceptualization. **Alessandro Gasparetto:** Writing – review & editing, Supervision, Project administration, Funding acquisition.

Declaration of competing interest

The authors declare that they have no known competing financial interests or personal relationships that could have appeared to influence the work reported in this paper.

Acknowledgments

The authors thank Mr. Baptiste Lesquerré-Caudebez for his help with the data collection and Prof. Paolo Sivilotti for allowing us to perform experiments in the vineyard of Azienda Agraria A. Servadei of the University of Udine (Italy). The first author acknowledges support from the National Ph.D. Programme in Artificial Intelligence of University of Naples Federico II (Italy). This research was developed within the Laboratory for Artificial Intelligence for Human–Robot Collaboration (AI4HRC) funded by Fondazione Friuli, and the Laboratory for Big Data, IoT, Cyber Security (LABIC) funded by Friuli Venezia Giulia region. This work was carried out within the Agritech National Research Center and received funding from the European Union Next-Generation EU (Piano Nazionale di Ripresa e Resilienza (PNRR) – Missione 4 Componente 2, Investimento 1.4 - D.D. 1032 17/06/2022, CN00000022). This manuscript reflects only the authors' views and opinions, neither the European Union nor the European Commission can be considered responsible for them.

Data availability

Data will be made available on request.

References

[1] J. Tardaguila, M. Stoll, S. Gutiérrez, T. Proffitt, M.P. Diago, Smart applications and digital technologies in viticulture: A review, Smart Agric. Technol. 1 (2021) 100005.

[2] A. Sairoel, G. Girma, A. Hassan Mohammed, Optimizing the performance of a wheeled mobile robots for use in agriculture using a linear-quadratic regulator, Robot. Auton. Syst. 174 (2024) 104642.

[3] D. Tiozzo Fasiolo, L. Scalera, E. Maset, A. Gasparetto, Towards autonomous mapping in agriculture: A review of supportive technologies for ground robotics, Robot. Auton. Syst. 169 (2023) 104514.

[4] M. Ammoniaci, S. Kartsiotis, R. Perria, P. Storchi, State of the art of monitoring technologies and data processing for precision viticulture, Agriculture 11 (3) (2021) 201.

[5] D. Tiozzo Fasiolo, A. Pichierri, P. Sivilotti, L. Scalera, An analysis of the effects of water regime on grapevine canopy status using a UAV and a mobile robot, Smart Agric. Technol. 6 (2023) 100344.

[6] E. Maset, L. Scalera, A. Beinat, D. Visintini, A. Gasparetto, Performance investigation and repeatability assessment of a mobile robotic system for 3D mapping, Robotics 11 (3) (2022) 54.

[7] R.R. Shamshiri, E. Navas, V. Dworak, F.A.A. Cheein, C. Weltzien, A modular sensing system with CANBUS communication for assisted navigation of an agricultural mobile robot, Comput. Electron. Agric. 223 (2024) 109112.

[8] I. Hrabar, J. Goričanec, Z. Kovačić, Towards autonomous navigation of a mobile robot in a steep slope vineyard, in: 2021 44th International Convention on Information, Communication and Electronic Technology, MIPRO, IEEE, 2021, pp. 1119–1124.

[9] R. Bertoglio, V. Carini, S. Arrigoni, M. Matteucci, A Map-Free LiDAR-based system for autonomous navigation in vineyards, in: 2023 European Conference on Mobile Robots, ECMR, IEEE, 2023, pp. 1–6.

[10] M. Mammarella, L. Comba, A. Biglia, F. Dabbene, F. Gay, Cooperation of unmanned systems for agricultural applications: A case study in a vineyard, Biosyst. Eng. 223 (2022) 81–102.

[11] T. Schönegg, T. Tuna, F. Yang, G. Waibel, M. Mattamala, M. Hutter, Global path planning for autonomous vehicles in orchards and vineyards, in: 2024 13th International Workshop on Robot Motion and Control, RoMoCo, IEEE, 2024, pp. 1–8.

[12] R. Polvara, S. Molina, I. Hroob, A. Papadimitriou, K. Tsiolis, D. Giakoumis, S. Likothanassis, D. Tzovaras, G. Cielniak, M. Hanheide, Bacchus Long-Term (BLT) data set: Acquisition of the agricultural multimodal BLT data set with automated robot deployment, J. Field Robot. (2023).

[13] L.C. Santos, A.S. Aguiar, F.N. Santos, A. Valente, J.B. Ventura, A.J. Sousa, Navigation stack for robots working in steep slope vineyard, in: Proceedings of SAI Intelligent Systems Conference, Springer, 2020, pp. 264–285.

[14] S. Cerrato, D. Aghi, V. Mazzia, F. Salvetti, M. Chiaberge, An adaptive row crops path generator with deep learning synergy, in: 2021 6th Asia-Pacific Conference on Intelligent Robot Systems, ACIRS, IEEE, 2021, pp. 6–12.

[15] A. Ravankar, A.A. Ravankar, A. Rawankar, Y. Hoshino, Autonomous and safe navigation of mobile robots in vineyard with smooth collision avoidance, Agriculture 11 (10) (2021) 954.

[16] A. Silva Aguiar, F. Neves Dos Santos, J. Cunha Boaventura, H. Sobreira, A. Jorge Sousa, Localization and mapping on agriculture based on point-feature extraction and semiplanes segmentation from 3D LiDAR data, Front. Robot. AI 9 (2022) 832165.

[17] T. Clamens, G. Alexakis, R. Duverne, R. Seulin, E. Fauvet, D. Fofi, Real-time multispectral image processing and registration on 3D point cloud for vineyard analysis, in: 16th International Conference on Computer Vision Theory and Applications, 2021.

[18] F. Crocetti, E. Bellocchio, A. Dionigi, S. Felicioni, G. Costante, M. Fravolini, P. Valigi, ARD-VO: Agricultural robot data set of vineyards and olive groves, J. Field Robot. 40 (6) (2023) 1678–1696.

[19] J. Fernández-Novales, V. Saiz-Rubio, I. Barrio, F. Rovira-Más, A. Cuenca-Cuenca, F. Santos Alves, J. Valente, J. Tardaguila, M. Diago, Monitoring and mapping vineyard water status using non-invasive technologies by a ground robot, Remote. Sens. 13 (14) (2021) 2830.

[20] M. Marzoa Tanco, G. Trinidad Barnech, F. Andrade, J. Baliosian, M. LLofriu, J. Di Martino, G. Tejera, Magro dataset: A dataset for Simultaneous Localization and Mapping in agricultural environments, Int. J. Robot. Res. 43 (5) (2024) 591–601.

[21] M. Chakraborty, L. Khot, S. Sankaran, P. Jacoby, Evaluation of mobile 3D light detection and ranging based canopy mapping system for tree fruit crops, Comput. Electron. Agric. 158 (2019) 284–293.

[22] A. Silwal, F. Yandun, A.K. Nellithimaru, T. Bates, G. Kantor, Bumblebee: A path towards fully autonomous robotic vine pruning., Field Robot. 2 (1) (2022) 1661–1696.

[23] I. Hroob, R. Polvara, S. Molina, G. Cielniak, M. Hanheide, Benchmark of visual and 3D LiDAR SLAM systems in simulation environment for vineyards, in: Annual Conference Towards Autonomous Robotic Systems, Springer, 2021, pp. 168–177.

[24] P. Astolfi, A. Gabrielli, L. Bascetta, M. Matteucci, Vineyard autonomous navigation in the Echord++ GRAPE experiment, IFAC-PapersOnLine 51 (11) (2018) 704–709.

[25] G. Peng, J. Junsheng, S. Jian, X. Fuxiang, B. Yang, Y. Fu, Z. Wang, X. Zheng, S. Xie, B. Li, Canopy volume measurement of fruit trees using robotic platform loaded LiDAR data, IEEE Access 9 (2021) 156246–156259.

[26] I. Hroob, S. Molina, R. Polvara, G. Cielniak, M. Hanheide, Adaptive robot localization in dynamic environments through self-learnt long-term 3D stable points segmentation, Robot. Auton. Syst. (2024) 104786.

[27] J. Cremona, R. Comelli, T. Pire, Experimental evaluation of visual-inertial odometry systems for arable farming, J. Field Robot. 39 (7) (2022) 1121–1135.

[28] T. Lowe, P. Moghadam, E. Edwards, J. Williams, Canopy density estimation in perennial horticulture crops using 3D spinning LiDAR SLAM, J. Field Robot. 38 (4) (2021) 598–618.

[29] S. Pasinetti, M. Maesano, E. Brunori, F.V. Moresi, A. Bernardini, P. Cirenei, R. Biasi, Introducing on-the-go sensing rover for vines canopy abiotic stressors detection, in: 2022 IEEE Workshop on Metrology for Agriculture and Forestry, MetroAgriFor, IEEE, 2022, pp. 208–212.

[30] G. Ristorto, R. Gallo, A. Gasparetto, L. Scalera, R. Vidoni, F. Mazzetto, A mobile laboratory for orchard health status monitoring in precision farming, Chem. Eng. Trans. 58 (2017) 661–666.

[31] H. Teng, Y. Wang, X. Song, K. Karydis, Multimodal dataset for localization, mapping and crop monitoring in citrus tree farms, in: International Symposium on Visual Computing, 2023, pp. 571–582.

[32] ROS, Carrot Planner, 2018, https://wiki.ros.org/carrot_planner.

[33] D. Fox, W. Burgard, S. Thrun, The Dynamic Window Approach to collision avoidance, IEEE Robot. Autom. Mag. 4 (1) (1997) 23–33.

[34] T. Shan, B. Englot, D. Meyers, W. Wang, C. Ratti, D. Rus, LIO-SAM: Tightly-coupled LiDAR inertial odometry via smoothing and mapping, in: 2020 IEEE/RSJ International Conference on Intelligent Robots and Systems, IROS, 2020, pp. 5135–5142.

[35] D. Tiozzo Fasiolo, L. Scalera, E. Maset, Comparing LiDAR and IMU-based SLAM approaches for 3D robotic mapping, Robotica 41 (9) (2023) 2588–2604.

[36] F. Crosilla, A. Beinat, A. Fusiello, E. Maset, D. Visintini, Orthogonal Procrustes Analysis, Adv. Procrustes Anal. Model. Photogramm. Comput. Vis. (2019) 7–28.

[37] D. Claus, A. Fitzgibbon, A rational function lens distortion model for general cameras, in: 2005 IEEE Computer Society Conference on Computer Vision and Pattern Recognition, Vol. 1, CVPR, IEEE, 2005, pp. 213–219.

[38] E. Maset, L. Magri, I. Toschi, A. Fusiello, Bundle block adjustment with constrained relative orientations, ISPRS Ann. Photogramm. Remote. Sens. Spat. Inf. Sci. 5 (2) (2020) 49–55.

[39] Micasense, Imageprocessing, 2024, https://github.com/micasense/imageprocessing?tab=readme-ov-file.

[40] A. Papadimitriou, I. Kleitsiotis, I. Kostavelis, I. Mariolis, D. Giakoumis, S. Likothanassis, D. Tzovaras, Loop closure detection and SLAM in vineyards with deep semantic cues, in: 2022 International Conference on Robotics and Automation, ICRA, IEEE, 2022, pp. 2251–2258.

Diego Tiozzo Fasiolo studied Mechanical Engineering at University of Padova (Italy), where he received his Bachelors Degree in 2019, and his Masters Degree in 2021. From 2021 to 2024 he worked at University of Udine (Italy) as a Ph.D. student of the Italian National Doctorate in Artificial Intelligence for Agriculture (Agrifood) and Environment coordinated by the University of Naples Federico II (Italy), and he achieved his Ph.D. in 2025. In 2024 he was a visiting Ph.D. student at the Stevens Institute of Technology in Hoboken (NJ, USA). In 2025 he was a Post Doc Research Fellow at University of Udine. His research interests are in the fields of mobile robotics, autonomous navigation, and 3D mapping.

Lorenzo Scalera achieved the Masters degree in Mechanical Engineering (cum laude) at University of Trieste in 2015, and the Ph.D. in Industrial and Information Engineering at University of Udine (Italy) in 2019. In 2018 he was a visiting Ph.D. student at the Stevens Institute of Technology in Hoboken (NJ, USA). In 2019 he was a Post Doc Research Fellow at Free University of Bozen-Bolzano (Italy). From 2020 to 2024 he was Assistant Professor of Mechanics of Machines at the Polytechnic Department of Engineering and Architecture of the University of Udine. Since 2024 he is Associate Professor at University of Udine. He currently serves in the Editorial Board of IEEE Robotics and Automation

Letters. He is author of more than 100 international publications in scientific journals and conferences. His research interests include dynamic modeling of mechatronic and robotic systems, trajectory planning, collaborative robotics, and mobile robotics.

Eleonora Maset received the Master's Degree in Environmental Engineering (cum laude) in 2015, and the Ph.D. degree in Industrial and Information Engineering from the University of Udine (Italy), in 2019. She currently holds a post-doctoral position at the Polytechnic Department of Engineering and Architecture, University of Udine. Her research interests include image orientation, point cloud processing, indoor modeling, and mobile robotics.

Alessandro Gasparetto received the M.Sc. in Electronic Engineering from the University of Padova, Italy, in 1992; the M.Sc. in Mathematics from University of Padova, Italy, in 2003; the Ph.D. in Mechanics of Machines from University of Brescia, Italy, in 1996. He is Full Professor of Mechanics of Machines at the Polytechnic Department of Engineering and Architecture, University of Udine (Udine, Italy), where he is the head of the research group in Mechatronics and Robotics, as well as the Head of the Department (since 2021). He has been included in the ranking of the top 2 quoted and authoritative scientists in the world, published by researchers at Stanford University (2019 and 2021). Since 2017, he is the Chair of IFToMM Italy, the Italian branch of IFToMM (the International Federation for the Promotion of Mechanism and Machine Science). Since 2018, he is the Chair of the IFToMM Permenent Commission for the History of Mechanism and Machine Science. His research interests are in the fields of modeling and control of mechatronic systems, robotics, mechanical design, industrial automation, mechanical vibrations. He is author of more than 200 international publications and has been involved in the scientific and organizing committees of several conferences, as well as in many research projects, at the regional, national and European level.